Received: 18 January 2023 | Revised: 30 November 2023 | Accepted: 6 December 2023

DOI: 10.1002/mp.16914

RESEARCH ARTICLE

MEDICAL PHYSICS

Strategies for deep learning-based attenuation and scatter correction of brain ^{18}F-FDG PET images in the image domain

Reza Jahangir[1] | **Alireza Kamali-Asl**[1] | **Hossein Arabi**[2] | **Habib Zaidi**[2,3,4,5]

[1]Department of Medical Radiation Engineering, Shahid Beheshti University, Tehran, Iran

[2]Division of Nuclear Medicine and Molecular Imaging, Geneva University Hospital, Geneva, Switzerland

[3]Geneva University Neurocenter, Geneva University, Geneva, Switzerland

[4]Department of Nuclear Medicine and Molecular Imaging, University of Groningen, University Medical Center Groningen, Groningen, Netherlands

[5]Department of Nuclear Medicine, University of Southern Denmark, Odense, Denmark

Correspondence
Alireza Kamali-Asl, Department of Medical Radiation Engineering, Shahid Beheshti University, Tehran, Iran.
Email: a_kamali@sbu.ac.ir

Funding information
Swiss National Science Foundation, Grant/Award Number: SNSF 320030_176052; Private Foundation of Geneva University Hospitals, Grant/Award Number: RC-06–01

Abstract

Background: Attenuation and scatter correction is crucial for quantitative positron emission tomography (PET) imaging. Direct attenuation correction (AC) in the image domain using deep learning approaches has been recently proposed for combined PET/MR and standalone PET modalities lacking transmission scanning devices or anatomical imaging.

Purpose: In this study, different input settings were considered in the model training to investigate deep learning-based AC in the image space.

Methods: Three different deep learning methods were developed for direct AC in the image space: (i) use of non-attenuation-corrected PET images as input (NonAC-PET), (ii) use of attenuation-corrected PET images with a simple two-class AC map (composed of soft-tissue and background air) obtained from NonAC-PET images (PET segmentation-based AC [SegAC-PET]), and (iii) use of both NonAC-PET and SegAC-PET images in a Double-Channel fashion to predict ground truth attenuation corrected PET images with Computed Tomography images (CTAC-PET). Since a simple two-class AC map (generated from NonAC-PET images) can easily be generated, this work assessed the added value of incorporating SegAC-PET images into direct AC in the image space. A 4-fold cross-validation scheme was adopted to train and evaluate the different models based using 80 brain ^{18}F-Fluorodeoxyglucose PET/CT images. The voxel-wise and region-wise accuracy of the models were examined via measuring the standardized uptake value (SUV) quantification bias in different regions of the brain.

Results: The overall root mean square error (RMSE) for the Double-Channel setting was 0.157 $\pm$ 0.08 SUV in the whole brain region, while RMSEs of 0.214 $\pm$ 0.07 and 0.189 $\pm$ 0.14 SUV were observed in NonAC-PET and SegAC-PET models, respectively. A mean SUV bias of 0.01 $\pm$ 0.26% was achieved by the Double-Channel model regarding the activity concentration in cerebellum region, as opposed to 0.08 $\pm$ 0.28% and 0.05 $\pm$ 0.28% SUV biases for the network that uniquely used NonAC-PET or SegAC-PET as input, respectively. SegAC-PET images with an SUV bias of -1.15 $\pm$ 0.54%, served as a benchmark for clinically accepted errors. In general, the Double-Channel network, relying on both SegAC-PET and NonAC-PET images, outperformed the other AC models.

Conclusion: Since the generation of two-class AC maps from non-AC PET images is straightforward, the current study investigated the potential added value of incorporating SegAC-PET images into a deep learning-based direct AC approach. Altogether, compared with models that use only NonAC-PET and SegAC-PET images, the Double-Channel deep learning network exhibited superior attenuation correction accuracy.

KEYWORDS
attenuation correction, deep learning, PET, quantitative imaging, radiomics

1 | INTRODUCTION

Positron emission tomography (PET), as a non-invasive functional modality, provides 3-D biodistribution maps of radioactive tracers at the molecular and cellular levels. This enables non-invasive in-vivo estimation of chemical and biological processes within organs/tissues. Most neuroimaging PET studies employ ^{18}F-Fluorodeoxyglucose (FDG) radiotracer for the diagnosis of neurodegenerative diseases owing to its close correlation with cerebral glucose metabolism. In hybrid PET/computed tomography (CT) scanners, CT images are employed on virtually all commercial systems to model/compensate for the physical degrading factors including scattered and attenuated photons in PET. However, some scatter correction approaches, such as energy-based scatter correction,[1–5] do not require CT/transmission images or other structural information.

For PET attenuation and scatter correction, anatomical CT images can be readily exploited in combined PET/CT scanners. However, hybrid PET/magnetic resonance (MR) imaging devices face the challenge of generating patient-specific attenuation maps based on magnetic resonance images.[6] This stems from the fact that MR intensity reflects proton density rather than electron density, required in PET attenuation and scatter correction. Furthermore, attenuation and scatter correction in standalone PET scanners, designed and fabricated for brain imaging, is the major barrier to accurate quantitative PET imaging and reliable diagnosis.[7] Though these dedicated PET scanners provide relatively higher sensitivity and spatial resolution, in comparison with the conventional PET/CT or PET/MR systems, they are not commonly combined with anatomical/structural imaging modality.[8,9] Hence, the generation of attenuation maps or accounting for attenuated/scattered photons is not a trivial task.[10] Conventional strategies for the generation of AC maps in dedicated-brain PET imaging involve contouring the non-AC PET images and assigning predefined attenuation coefficients to soft tissue and bone[11,12] or atlas registration, which relies on paired datasets of head templates to identify the underlying anatomical structures.[13–15] Moreover, simultaneous reconstruction of activity and attenuation maps enables PET AC without using transmission data.[16–18] The advent of deep learning algorithms has enabled the development of novel approaches for generating synthetic CT from non-AC images,[19–21] estimating attenuation correction information from PET emission data,[22–24] or applying attenuation correction on PET images using hybrid methods, such as combining deep learning, joint attenuation and activity map reconstruction.[25,26]

In addition to these approaches, direct application of AC on PET images before attenuation and scatter correction (NonAC-PET) without employing structural information has shown promising results.[10,23,27–28] To this end, a deep learning network is trained to predict attenuation and scatter-corrected PET images from NonAC-PET images using CT-based AC (CTAC-PET) as ground truth. Furthermore, a segmentation-based attenuation correction technique, implemented on commercial systems, including the Philips whole-body Ingenuity TF PET/MRI,[29] was employed as a silver standard providing the bottom line of a clinically acceptable performance expectation.[24,10,28–29] In this regard, a simple PET attenuation map containing only water-equivalent attenuating medium can be generated by segmenting the subject outline from NonAC-PET images and assigning predefined air and soft-tissue attenuation coefficients to each voxel outside and inside of the subject outline, respectively. The generation of such AC maps does not require anatomical imaging, and can be simply conducted from NonAC-PET images with time-of-flight (TOF) information owing to the high signal-to-noise ratio and relatively strong contrast at the boundary of the body.[30] This approximate attenuation map can be used for preliminary PET AC, and a deep learning network can then be trained on the resultant segmentation-based attenuation corrected PET images (SegAC-PET) in order to predict accurate PET AC images based on these segmentations. Since the attenuation and scatter correction was partly/approximately applied to these PET images, the prediction of accurate PET AC images might be less challenging and/or more robust for deep learning approaches.

In this study, the use of a suboptimal attenuation correction on PET data was investigated in the direct PET AC through the assessment of different scenarios based on a deep learning approach. These scenarios include: (i) direct PET AC prediction from NonAC-PET images, (ii) PET AC prediction from SegAC-PET images, and (iii) PET AC prediction from a Double-Channel deep learning approach using SegAC-PET and NonAC-PET images simultaneously as inputs.

2 | MATERIALS AND METHODS

2.1 | PET/CT data acquisition

The assessment of direct AC in the image space was conducted retrospectively on 80 participants who had undergone TOF brain PET/CT examinations. The entire patient group provided informed consent as required by

Geneva University Hospitals' Ethics Committee for this study. A total of 44 males and 36 females were involved in this work having a mean weight and age of 73 ± 18 kg and 66 ± 11 years, respectively. PET/CT brain data were acquired on a Biograph mCT scanner (Siemens Healthcare) from a 20-min scan in a single bed position. A low-dose CT imaging (using setting parameters of 120 kVp, 20 mAs, speed 0.3 s/rotation, voxel size 0.9 × 0.9 × 2.5 mm^3) was performed for PET AC. PET acquisitions started 33 ± 5 min following the injection of 206 ± 12.95 MBq of ^{18}F-FDG.

2.2 | Data preparation

Direct application of AC on PET images in the image space was investigated for three different strategies: (i) use of NonAC-PET images as the input, (ii) use of SegAC-PET images as the input, and (iii) use of NonAC-PET and SegAC-PET images together in a double-input mode to estimate PET AC images. To train the deep learning models, a dataset consisting of NonAC-PET, SegAC-PET, and CTAC-PET images was created. To this end, the raw PET data reconstruction was performed using Siemens e7 tool with and without CT-derived attenuation maps to produce CTAC-PET (reference image) and NonAC-PET images using TOF 3-D ordinary Poisson ordered subsets-expectation maximization (5 iterations; 21 subsets; 200 × 200 × 109 matrix size; 2 × 2 × 2 mm^3 voxel size; 2 mm Gaussian post-reconstruction filter).

A two-class attenuation map was generated from TOF non-AC PET data by applying slice-by-slice head contouring to produce SegAC-PET images. To achieve this, an empirical 2-D intensity thresholding scheme was considered to discriminate between background air and the head region. The TOF non-AC PET images were converted into SUV units and then an SUV threshold of 0.4 was used for head contour detection. The final head contour was slightly smoothed in 3-D to eliminate cross-slice fluctuations. The outcome to this segmentation process is a binary mask of the head region, wherein attenuation coefficients of 0.0 cm^{-1} (≈−1000 Hounsfield Units) and 0.1 cm^{-1} (≈0 Hounsfield Units) were assigned to voxels within background air and head regions, respectively. Finally, SegAC-PET images were generated by reconstructing PET raw data using the aforementioned settings and the segmentation-based AC maps.

Sinogram data were created using Fourier rebinning (FORE) and TOF information into 13 TOF time bins. The single-scatter simulation technique was used within the reconstruction of CTAC-PET and SegAC-PET images. In the single-scatter simulation (SSS) correction approach,[31] the modeled coincidence events are compared with the measured coincidence events to estimate the contribution of scattered photons. To this end, an analytical model based on Klein–Nishina formula is applied to TOF PET data to estimate the scatter distribution and factors for each line of response (LOR) and TOF bin, adopting a grid space size of 1.75 cm in the transaxial direction and 2 cm in the axial direction.[32] To accurately calculate the scatter fraction, a tail fitting algorithm is employed to estimate the percentage of scattered events in the photopeak window based on the fitted scatter distribution to the detected events outside the body contour. Furthermore, the body contour extracted from the CT-based attenuation correction (AC) map served as the foundation for the calculation of the scatter component. This calculation utilized a tail fitting algorithm, incorporating a margin of 2 mm. To effectively eliminate scattered photons, an energy window ranging between 435 and 650 keV was employed.[32] Based on this calculation, the average scatter fraction for CT-based AC and SegAC was 24.8 ± 5% and 23.4 ± 6%, respectively.

PET images' intensities should be normalized to a common range prior to the deep learning model training to facilitate/harmonize the process of feature extraction. This was accomplished by first converting the CTAC-PET, SegAC-PET, and NonAC-PET voxel intensities into SUVs, then an empirical fixed value of 9 was used to scale down the intensities of CTAC-PET and SegAC-PET images. Likewise, NonAC-PET images were normalized by an empirical factor of 3. In an effort to diminish the computation burden, background air was cut off from PET images, leading to a final matrix size of 64 × 64 × 104 voxels.

2.3 | Deep learning architecture

Niftynet, a dedicated platform for implementing deep learning algorithms, was exploited for the realization of direct AC. This platform provides modular convolutional neural network architectures for common medical image analysis.[33] The Niftynet platform was built in Python using the TensorFlow libraries. A high-resolution, compact convolutional network[34] known as HighResNet (in the Niftynet platform) was retrieved and re-configured in order to achieve direct PET AC estimation from NonAC-PET or SegAC-PET images.

This neural network extracts image features at various scales/levels by using 20 residual layers while preserving the spatial resolution of the input image by applying dilated convolution operations. For low-level feature extraction such as edges, convolutional kernels of 3 × 3 voxels were employed in the initial seven convolution layers. These convolutional filters use dilation factors of 2 and 4 in the next seven and six layers to extract medium- and low-level image features, respectively. A residual connection is then established to link every two convolutional layers to form a residual block, wherein a rectified linear unit (ReLU) activation function

is followed by a batch normalization. The architecture of this network is presented in Figure S1.

As mentioned earlier, three scenarios were followed for the implementation of direct AC in the image space: prediction of CTAC-PET from NonAC-PET images, SegAC-PET images, and both NonAC-PET and SegAC-PET (using a Double-Channel input) images. A 4-fold cross-validation framework was followed for the implementation of each scenario considering that 80 subjects were selected at each fold in the dataset, 60 training, and 20 test subjects. The training of the deep learning models was performed in 2-D mode using 60 × 104 (Number of subjects × Number of slices) training samples.

In the Niftynet platform, the residual neural network was implemented and trained with a 64 × 64 spatial window, a learning rate of 0.001, the L2norm loss function, the Adam optimizer, a decay of 0.0001, batch size of 30, and a sample per volume of 1. The three AC models were trained and inferred in a 2-D mode. Training of the models was performed in 20 epochs taking 9.7 h to reach the plateau of the training loss function. The models' training and inference were conducted on the NVIDIA GTX 1060 (GPU memory of 6 GB) and the Linux Ubuntu 18.04 LTS operating system. No transfer learning or pre-trained model was used within the training of these models. The inference of the synthetic CTAC-PET images took 2.8 s for each patient (one-bed position, whole-brain study).

2.4 | Evaluation strategy

The performance of the different scenarios for direct AC was assessed against CT-based AC considered as a reference/standard. Moreover, SegAC-PET images, which provide a bottom line for clinically acceptable errors, were included in this evaluation. The two-class SegAC obtained from the classification of TOF NonAC-PET images is considered a proxy for MRI-guided attenuation map generation implemented on some commercial PET/MRI scanners.[28]

Regarding CTAC-PET images as standard of reference, the mean error (ME), mean absolute error (MAE), and root mean square error (RMSE) in terms of SUV, together with a peak signal-to-noise ratio (PSNR), and structural similarity index measure (SSIM) were calculated for the different PET images using Equations (1)–(5), respectively. The synthetic CTAC-PET images estimated by the deep learning models from NonAC-PET images, SegAC-PET images, and both NonAC-PET and SegAC-PET images (Double-Channel input) are referred to as DEEP-NAC, DEEP-Seg, and DEEP-DC, respectively.

$$ME = \frac{1}{V}\sum_{q=1}^{V}\left(PET_{ASC}(q) - PET_{Ref}(q)\right) \quad (1)$$

$$MAE = \frac{1}{V}\sum_{q=1}^{V}\left|PET_{ASC}(q) - PET_{Ref}(q)\right| \quad (2)$$

$$RSME = \sqrt{\frac{1}{V}\sum_{q=1}^{V}\left(PET_{ASC}(q) - PET_{Ref}(q)\right)^2} \quad (3)$$

$$PSNR = 20\log_{10}\frac{\max(PET_{Ref} \cup PET_{ASC})}{\sqrt{MSE(PET_{ASC} \cap PET_{Ref})}} \quad (4)$$

$$SSIM = \frac{(2\mu_{Ref}\mu_{ASC} + c_1)(2\sigma_{Ref,ASC} + c_2)}{(\mu_{Ref}^2 + \mu_{ASC}^2 + c_1)(\sigma_{Ref}^2 + \sigma_{ASC}^2 + c_2)} \quad (5)$$

Here PET_{ASC} represents either SegAC-PET or PET images synthesized by the deep learning-based AC models and PET_{Ref} refers to the reference CTAC-PET images.

For region-based analysis of ^{18}F-FDG uptake, the radiotracer uptake was estimated in 70 brain regions using the digital atlas of the human brain and automated anatomical labels[35] implemented in the PMOD processing platform (version 3.8, PMOD Technologies Ltd., Zürich, Switzerland). An example of these brain regions overlaid on a CTAC-PET image is provided in Figure S2. For each of the 70 anatomical regions of the brain, the mean relative and absolute (%) bias (*RB* and *ARB*) across the 80 patients were computed using Equations (6) and (7), respectively. Given the activity concentration in the 70 brain regions for different PET images, the Bland-Altman plot of uptake differences with reference CTAC-PET images in SUV units was plotted for the different PET images. All quantitative metrics were calculated on 3-D volumes.

$$RB_{region}(\%) = \frac{(PET_{ASC})_{region} - (PET_{Ref})_{region}}{(PET_{Ref})_{region}} \times 100\% \quad (6)$$

$$ARB_{region}(\%) = \left|\frac{(PET_{ASC})_{region} - (PET_{Ref})_{region}}{(PET_{Ref})_{region}}\right| \times 100\% \quad (7)$$

Moreover, radiomic features of the 70 anatomical regions of the brain were extracted for all patients and different synthetic PET images using the LIFEx freeware radiomic feature calculation.[36] For each brain region, 28 radiomic features were extracted, including SUV, intensity, Grey-Level Run Length Matrix (GLRLM), Grey-Level Zone Length Matrix (GLZLM), and Grey-Level Co-occurrence Matrix (GLCM).

A voxel-wise joint histogram evaluation was performed to illustrate the correlation among the radiotracer distribution in CTAC-PET images and each synthetic PET image, including DEEP-NAC, DEEP-Seg, DEEP-DC, as well as SegAC-PET.

In order to determine the statistical significance of the differences between models, we conducted a paired *t*-test analysis for the different metrics, wherein statistical significance was defined at *P*-values less than 0.05.

TABLE 1 Quantitative evaluation of DEEP-NAC, DEEP-Seg, DEEP-DC, and SegAC-PET images within the whole brain region for 80 patients using CTAC-PET as ground truth.

	ME (SUV)	MAE (SUV)	RMSE (SUV)	PSNR (dB)	SSIM
DEEP-NAC	0.004 ± 0.09	0.152 ± 0.05	0.214 ± 0.07	19.08 ± 3.18	0.987 ± 0.01
DEEP-Seg	−0.008 ± 0.07	0.128 ± 0.08	0.189 ± 0.14	20.98 ± 3.68	0.990 ± 0.01
DEEP-DC	0.002 ± 0.06	0.123 ± 0.05	0.157 ± 0.08	21.48 ± 5.35	0.992 ± 0.01
SegAC-PET	−0.461 ± 0.08	0.483 ± 0.08	0.715 ± 0.14	17.24 ± 1.77	0.969 ± 0.01

Abbreviations: CTAC-PET, computed tomography-based attenuation correction-positron emission tomography; DC, Double Channel; MAE, mean absolute error; ME, mean error; NAC, non-attenuation-corrected; PSNR, peak signal-to-noise ratio; RMSE, root mean square error; SSIM, structural similarity index measure; SUV, standardized uptake value.

TABLE 2 *P*-values calculated between different AC methods for the quantitative metrics reported in Table 1.

	ME (SUV)	MAE (SUV)	RMSE (SUV)	PSNR (dB)	SSIM
DEEP-NAC vs. DEEP-Seg	0.44	< 0.02	< 0.05	< 0.01	< 0.02
DEEP-NAC vs. DEEP-DC	< 0.05	< 0.01	< 0.01	< 0.01	< 0.01
DEEP-NAC vs. SegAC-PET	< 0.01	< 0.01	< 0.01	< 0.01	< 0.01
DEEP-DC vs. DEEP-Seg	< 0.05	< 0.05	< 0.05	< 0.02	< 0.02
DEEP-Seg vs. SegAC-PET	< 0.01	< 0.01	< 0.01	< 0.01	< 0.01
DEEP-DC vs. SegAC-PET	< 0.01	< 0.01	< 0.01	< 0.01	< 0.01

Abbreviations: AC, attenuation correction; MAE, mean absolute error; ME, mean error; PSNR, peak signal-to-noise ratio; RMSE, root mean square error; SSIM, structural similarity index measure; SUV, standardized uptake value.

3 | RESULTS

The quantitative evaluation of DEEP-NAC, DEEP-Seg, DEEP-DC, as well as SegAC-PET images for the whole brain region is summarized in Table 1 wherein the average and standard deviation (SD) of different metrics are reported for all 80 patients. Estimation of CTAC-PET using the deep learning model taking NonAC-PET and SegAC-PET images simultaneously as input (noted as DEEP-DC), exhibited superior accuracy over the AC models taking NonAC-PET and SegAC-PET images independently (noted as DEEP-NAC and DEEP-Seg, respectively). However, all these three deep learning-based AC models were superior to SegAC-PET method. As shown in Table 2, there were statistically significant differences between these AC methods, particularly for MAE and RMSE metrics.

Representative views of attenuation corrected PET images using different AC techniques, together with the CTAC-PET images as reference and the corresponding bias/difference maps are shown in Figure 1.

A region-wise assessment of brain PET images transformed into a joint spatial map was performed to investigate the quantitative accuracy of the various AC strategies. The details of the region-based assessment of brain PET images are presented in Figures 2 and 3 wherein the average SUV bias and the average absolute SUV bias are reported for eight merged brain regions, including the cerebellum, temporal lobes, parietal lobes, thalamus, putamen, caudate nucleus, occipital lobes, and middle frontal lobes, separately for SegAC-PET, DEEP-NAC, DEEP-Seg, and DEEP-DC images. In these figures, the mean SUV bias is reported for all 80 patients. SegAC-PET images exhibited the highest SUV bias for most regions whereas DEEP-DC images exhibited below 3% absolute SUV bias across all regions. The results for the 70 brain regions across 80 patients are provided in Figures S3–S4.

In total, 28 major radiomic features were calculated for each of the 70 brain regions and the different PET images. The relative errors of these features were calculated concerning the reference radiomic features obtained from CTAC-PET images. Figures S5–S8 depict the relative errors of the 28 radiomic features for DEEP-DC, SegAC-PET, DEEP-NAC, and DEEP-Seg images, respectively.

The quantitative analysis of the activity distribution in the 70 anatomical brain regions for the different PET images is summarized in Bland-Altman plots presented in Figure 4. Less bias and variance were observed in DEEP-DC images compared to DEEP-Seg and SegAC-PET images. However, similar SUV bias and variance were seen in DEEP-NAC images. The regression plots in Figure 5 and voxel-wise joint histogram evaluation of PET images revealed the superior accuracy of the radiotracer recovery in DEEP-DC images wherein RMSE = 0.73 and $R^2 = 1$ were observed compared to RMSE = 1.29 and $R^2 = 0.977$, RMSE = 1.87 and $R^2 = -0.999$, and RMSE = 1.10 and $R^2 = 0.986$ obtained for SegAC-PET, DEEP-Seg, and DEEP-NAC, respectively.

4 | DISCUSSION

Attenuation correction based on deep learning approaches in PET imaging has recently attracted much attention resulting in the proposal of various strategies for indirect attenuation map generation and/or direct AC of PET images.[37–40] Among these

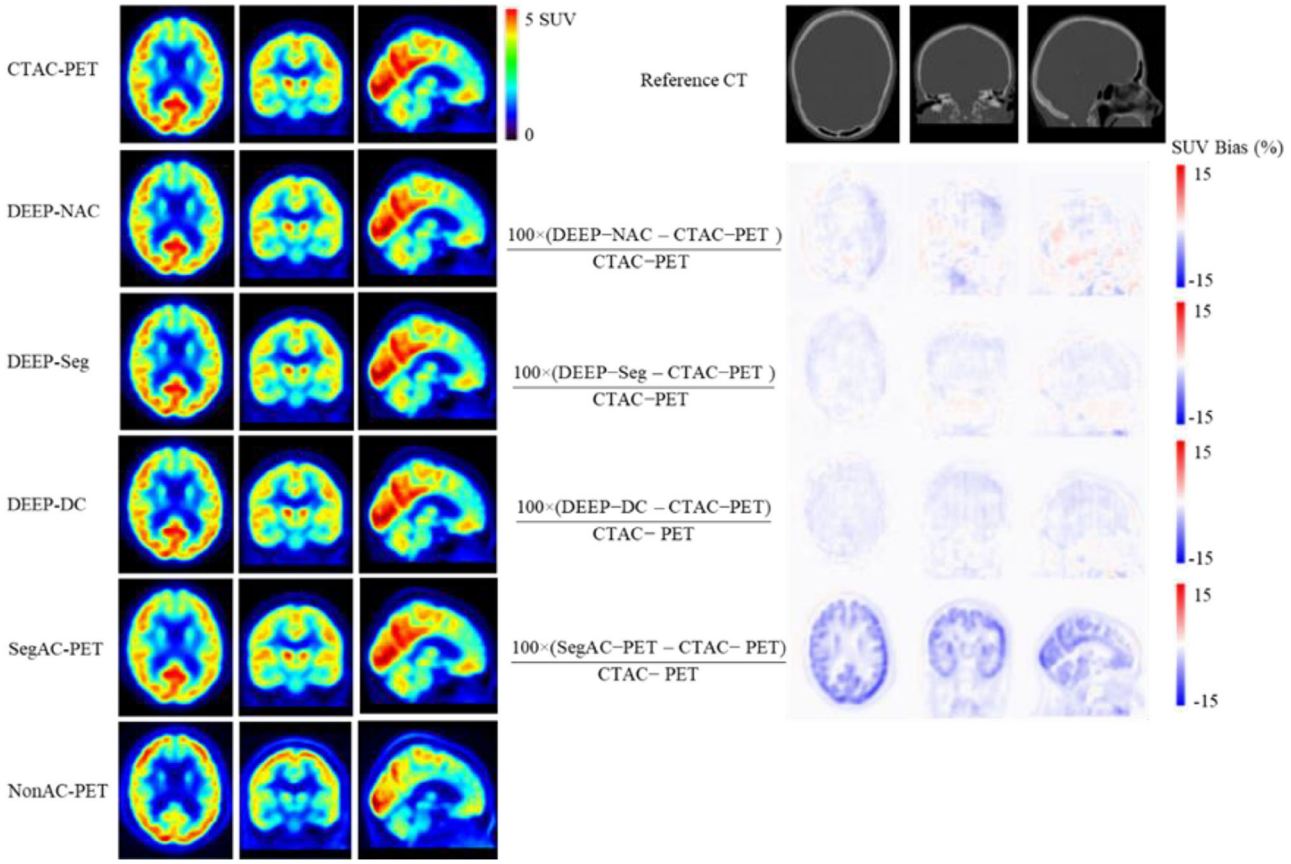

FIGURE 1 Representative transverse, sagittal, and coronal views of CTAC-PET, DEEP-NAC, DEEP-Seg, DEEP-DC), and SegAC-PET along with their corresponding CT images and bias maps considering CTAC-PET images as standard of reference. CTAC-PET, computed tomography-based attenuation correction-positron emission tomography; DC, Double Channel; NAC, non-attenuation-corrected.

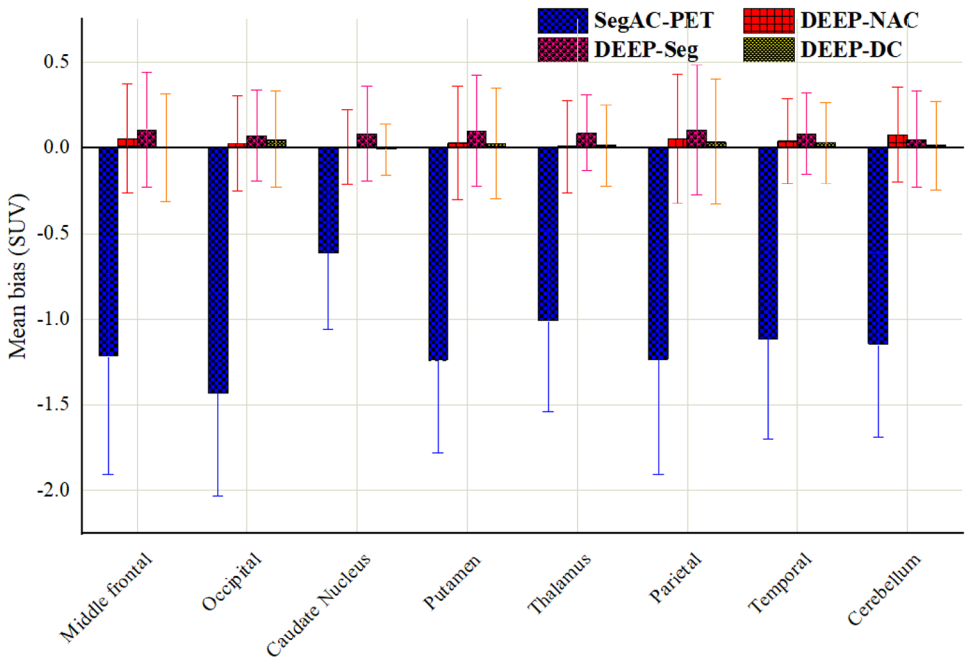

FIGURE 2 Mean standardized uptake value (SUV) bias of the radiotracer concentration calculated in eight merged brain regions across 80 subjects for the different attenuation correction (AC) approaches.

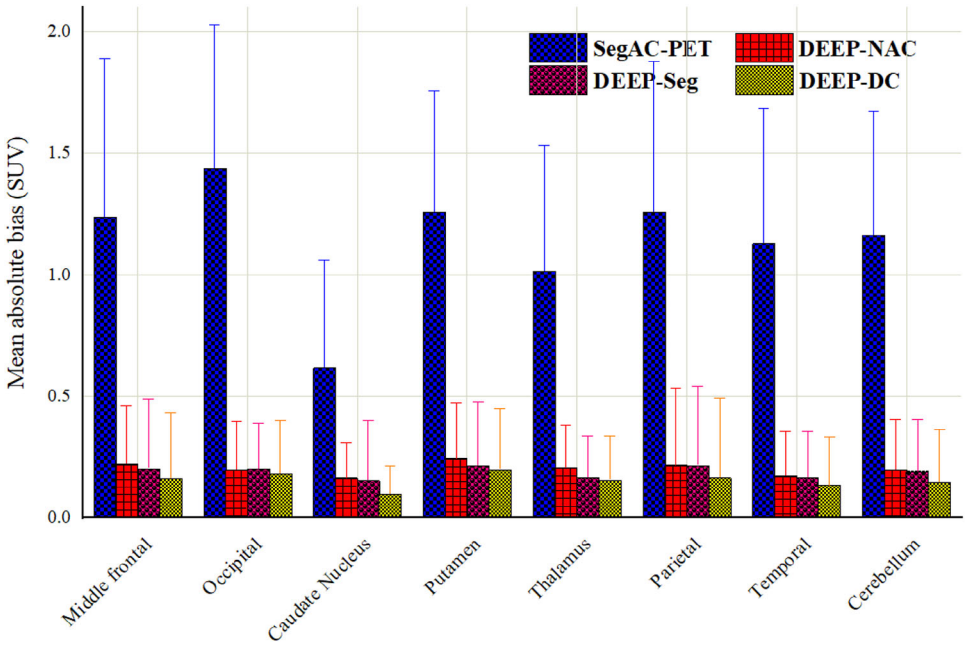

FIGURE 3 Mean absolute standardized uptake value (SUV) bias of the radiotracer concentration calculated in eight merged brain regions across 80 subjects for the different attenuation correction (AC) approaches.

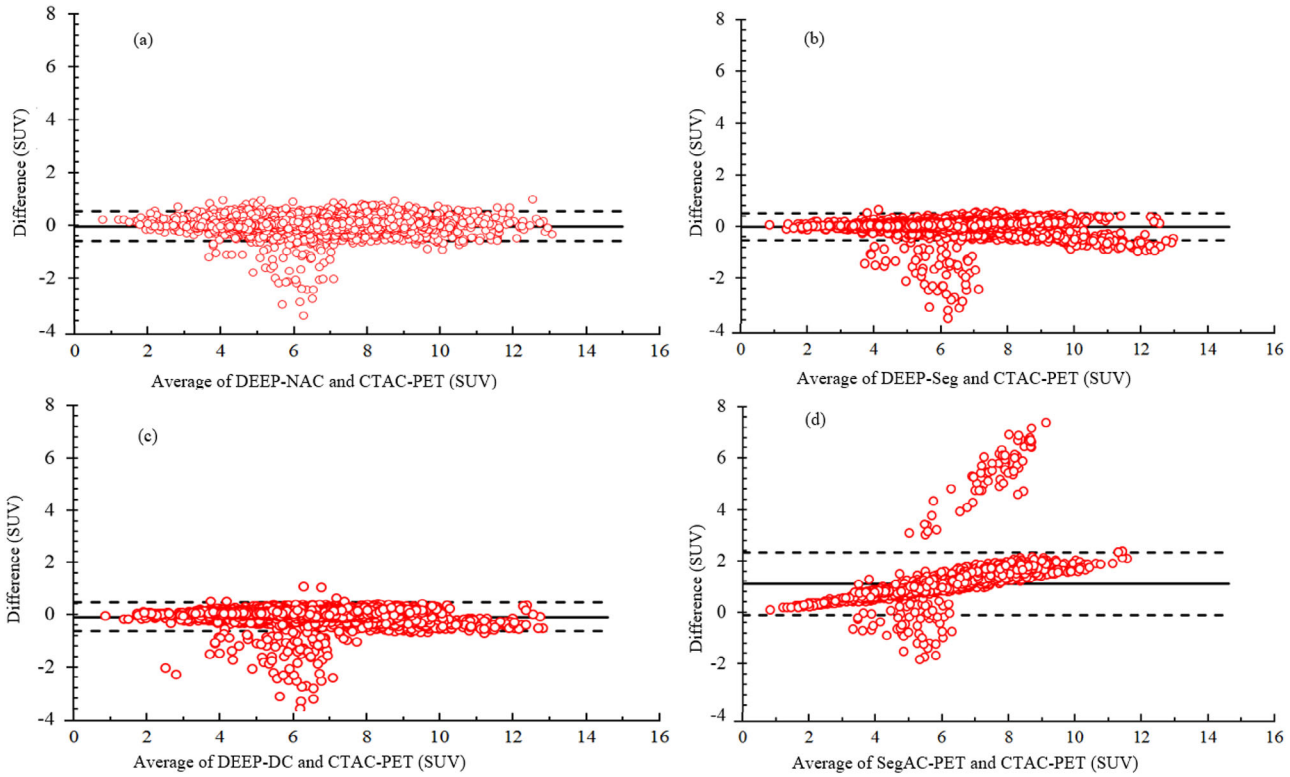

FIGURE 4 Bland-Altman plots of activity distribution in 70 anatomical regions of the brain estimated on (a) SegAC-PET, (b) DEEP-NAC, (c) DEEP-DC, and (d) DEEP-Seg images versus CTAC-PET images as ground truth. The average standardized uptake value (SUV) differences are specified by the solid lines, while the dashed lines show a 95% confidence interval (CI) of the SUV differences. CTAC, computed tomography-based attenuation correction; DC, Double Channel; NAC, non-attenuation-corrected; PET, positron emission tomography.

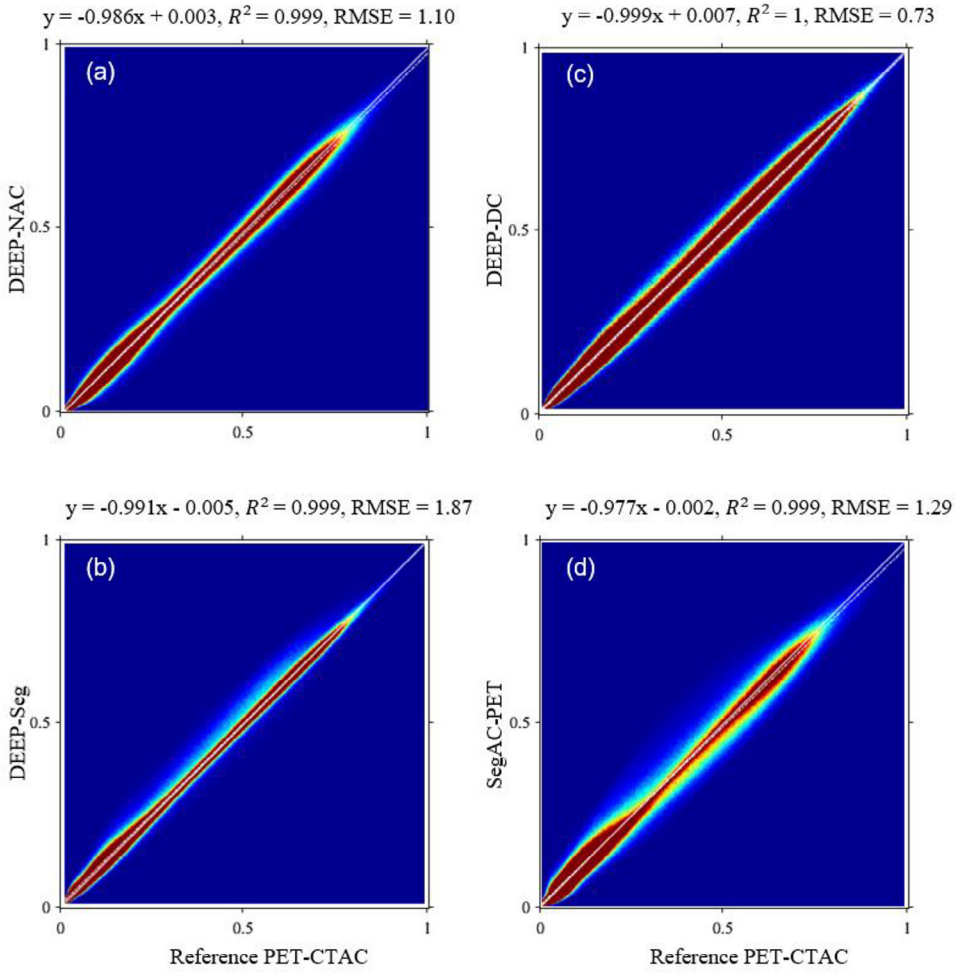

FIGURE 5 Joint histogram analysis of: (a) DEEP-NAC, (b) DEEP-Seg, (c) DEEP-DC, and (d) SegAC-PET images versus the reference CTAC-PET images. DC, Double Channel; NAC, non-attenuation-corrected; PET, positron emission tomography.

strategies, the direct application of AC on NonAC-PET images in the image domain is of particular interest. This approach does not require anatomical imaging, which is appealing for dedicated brain PET scanners. This approach is less sensitive to common sources of errors in conventional CT-based PET attenuation correction, for example mismatch between emission and transmission/MR images, body truncation, and inaccurate scatter correction.[10,27,41–43] In this regard, this study aimed to investigate the use of simple attenuation and scatter-corrected PET images to aid the direct application of AC in the image space. The motivation behind this investigation was that a simple two-class attenuation map can be simply generated from NonAC-PET images to reconstruct SegAC-PET images. This auxiliary attenuation map would be in perfect alignment with the emission data since it is generated directly from the PET data.

In this study, we assessed a segmentation-based method, a simplified approach encompassing air and water, synonymous with soft tissue. In the two-class attenuation correction (2-class AC) segmentation, bony structures were represented by a filling of soft tissue and/or water. Contrasting this, more sophisticated MR-guided AC methods have the capability to discern bony structures by establishing a distinct class for bone tissue. To showcase the efficacy of the Double-Channel direct, we conducted a comparative analysis with a segmentation approach that incorporates a separate class for bone tissue. For this purpose, patient CT images underwent segmentation into background air, soft tissue, and bony structures. The predefined attenuation values of 0.0 cm^{-1} (≈−1000 Hounsfield Units), 0.1 cm^{-1} (≈0 Hounsfield Units), and 0.125 cm^{-1} (≈460 Hounsfield Units) were assigned for background air, soft tissue, and bone, respectively.[25] This segmentation AC map, referred to as BoneAC, was juxtaposed against SegAC and DEEP-DC to underscore the superiority of the deep learning method. Table S1 provides a quantitative evaluation of DEEP-DC, BoneAC-PET, and SegAC-PET images across the entire brain region for 80 patients, using CTAC-PET as the ground truth. The

accompanying *P*-values in the table illuminate the superior performance of the deep learning approach in the image domain.

Segmentation-based methods involve assigning a predetermined attenuation coefficient to distinct tissue classes, disregarding the inherent variability in attenuation coefficients among different patients. In contrast, approaches that incorporate patient-specific attenuation coefficients in segmentation, particularly those accounting for bony structures, demonstrate a reduced bias compared to traditional methods. Deep learning techniques, in particular, have shown promise in mitigating segmentation errors by learning and adapting to the inherent variability in attenuation coefficients across individuals. This adaptability contributes to more accurate and patient-specific attenuation correction, presenting a notable advancement over rigid, predefined coefficient assignments.[26]

All three deep learning-based AC approaches evaluated in this study outperformed noticeably the segmentation-based AC map technique. The deep learning-based methods exhibited very close attenuation correction performances. However, the Double-Channel deep learning method simultaneously considering NonAC-PET and SegAC-PET images as input showed slightly superior accuracy, leading to an overall lower RMSE in the whole brain (Table 1) and voxel-wise analysis (Figure 5). The differences were statistically significant between the Double-Channel deep learning-based method and other methods for key metrics, such as the RMSE and the SUV bias in brain regions.

The two-class AC map is far from perfect. Nevertheless, it could help to partly compensate for the effect of attenuated and scattered photons on PET images. Therefore, the estimation of PET AC from SegAC-PET would face less complexity. However, relying only on SegAC-PET images has the drawback of losing the original information that lies in NonAC-PET images. In this regard, any errors in SegAC-PET images caused by miss-segmentation, erroneous AC map, or incorrect scatter correction would be reflected in the output of the deep learning method relying only on SegAC-PET images. A Double-Channel deep learning method could benefit from the information existing in the combination of NonAC-PET and SegAC-PET images. In this sense, SegAC-PET helps to reduce the complexity of the AC problem, and still the information lying in the original NonAC-PET images would aid the deep learning approach to find an optimal solution. Moreover, in the case of any error in SegAC-PET images, for example, due to miss-segmentation, NonAC-PET images have sufficient information for the prediction of an acceptable/tolerable CTAC-PET image.

The deep learning AC methods in this work are entirely automated and attenuation corrected images are directly inferenced from NonAC-PET images in a few seconds (2.1 s) within the image domain without the need for supplementary structural data. Considering that scatter correction using the single-scatter correction algorithm takes more than 1 min (up to 150 s) in TOF PET imaging,[10,44] the fast inference time of deep learning approaches would be considered an advantage for our methods.

Correction of scattered photons is a significant/important component of the AC process. Due to the model-based and analytic nature of scatter estimation, the scatter distribution and amplitude depend on the algorithm and parameters used for the calculation of scattered photons. In this regard, the training dataset for direct AC in the image domain should be created using the same scatter correction algorithm and parameters to avoid discrepancies between the different training subjects. Moreover, the same scatter correction setting should be employed for SegAC-PET images (to be used in the Double-Channel deep learning approach) to create a consistent model. Previous studies have shown that the estimation of scattered events (or generation of scattered sinogram) is not highly sensitive to slight modifications/simplifications in the attenuation maps. In this regard, the scatter estimation (scatter sinogram generation) from the reference CT image and a segmentation-based method, such as the two-class AC map, would be in high agreement (scatter fractions for CT-based AC and SegAC were 24.8 $\pm$ 5% and 23.4 $\pm$ 6%, respectively). Since SegAC-PET images contain almost complete/sufficient information about scattered events, the Double-Channel deep learning model would be able to offer an overall superior solution due to the reduced complexity of the AC problem.

5 | CONCLUSION

This work aimed to investigate the direct application of AC in the image space. This was achieved by training a deep learning network for direct AC using three different inputs, wherein the input of the network was assigned to a single NonAC-PET image, single SegAC-PET (obtained from NonAC-PET using an AC map including background air and soft-tissue), and the two NonAC-PET and SegAC-PET images in a Double-Channel model. In general, the Double-Channel deep learning approach which simultaneously took NonAC-PET and SegAC-PET images as input, exhibited superior accuracy for activity concentration retrieval in brain imaging. The Double-Channel deep learning approach led to an SUV bias of less than 4% in various regions of the brain, whereas the segmentation-based AC map led to an SUV bias of over 13%. The Double-Channel deep learning network, which relies on the two NonAC-PET and SegAC-PET images, would offer improved accuracy in AC modeling, compared to a model using only NonAC-PET or SegAC-PET images.

ACKNOWLEDGMENTS

This work was supported by the Swiss National Science Foundation under grant SNSF 320030_176052 and the Private Foundation of Geneva University Hospitals under grant RC-06−01.

CONFLICT OF INTEREST STATEMENT

The authors declare no conflicts of interest.

REFERENCES

1. Brusaferri L, Bousse A, Efthimiou N, et al. Potential benefits of incorporating energy information when estimating attenuation from PET data. Paper presented at: 2017 IEEE Nuclear Science Symposium and Medical Imaging Conference (NSS/MIC); October 21-28, 2017; Atlanta, GA.
2. Efthimiou N, Karp JS, Surti S. Data-driven, energy-based method for estimation of scattered events in positron emission tomography. *Phys Med Biol*. 2022;67(9):095010.
3. Brusaferri L, Bousse A, Emond EC, et al. Joint activity and attenuation reconstruction from multiple energy window data with photopeak scatter re-estimation in non-TOF 3-D PET. *IEEE Trans Radiat Plasma Med Sci*. 2020;4(4):410-421.
4. Hamill JJ. Phantom evaluation of energy-based scatter estimation in an SiPM PET scanner. Paper presented at: 2020 IEEE Nuclear Science Symposium and Medical Imaging Conference (NSS/MIC); October 31-November 7, 2020; Boston, MA.
5. Popescu LM, Lewitt RM, Matej S, Karp JS. PET energy-based scatter estimation and image reconstruction with energy-dependent corrections. *Phys Med Biol*. 2006;51(11):2919.
6. Mehranian A, Arabi H, Zaidi H. Vision 20/20: magnetic resonance imaging-guided attenuation correction in PET/MRI: challenges, solutions, and opportunities. *Med Phys*. 2016;43(3):1130-1155.
7. Wienhard K, Schmand M, Casey M, et al. The ECAT HRRT: performance and first clinical application of the new high resolution research tomograph. *IEEE Trans Nucl Sci*. 2002;49(1):104-110.
8. González AJ, Sánchez F, Benlloch JM. Organ-dedicated molecular imaging systems. *IEEE Trans Radiat Plasma Med Sci*. 2018;2(5):388-403.
9. Lee JS. Technical advances in current PET and hybrid imaging systems. *Open Nucl Med J*. 2010;2(192-208):14.
10. Yang J, Park D, Gullberg GT, Seo Y. Joint correction of attenuation and scatter in image space using deep convolutional neural networks for dedicated brain 18F-FDG PET. *Phys Med Biol*. 2019;64(7):075019.
11. Siegel S, Dahlbom M. Implementation and evaluation of a calculated attenuation correction for PET. *IEEE Trans Nucl Sci*. 1992;39(4):1117-1121.
12. Bergström M, Litton J, Eriksson L, Bohm C, Blomqvist G. Determination of object contour from projections for attenuation correction in cranial positron emission tomography. *J Comput Assist Tomogr*. 1982;6(2):365-372.
13. Yang J, Wiesinger F, Kaushik S, et al. Evaluation of sinus/edge-corrected zero-echo-time–based attenuation correction in brain PET/MRI. *J Nucl Med*. 2017;58(11):1873-1879.
14. Kops ER, Herzog H, Alternative methods for attenuation correction for PET images in MR-PET scanners. Paper presented at: 2007 IEEE Nuclear Science Symposium Conference Record; October 26-November 3, 2007; Honolulu, HI.
15. Sekine T, Buck A, Delso G, et al. Evaluation of atlas-based attenuation correction for integrated PET/MR in human brain: application of a head atlas and comparison to true CT-based attenuation correction. *J Nucl Med*. 2016;57(2):215-220.
16. Kobayashi T, Kitamura K, A solution for scaling problem in joint estimation of activity and attenuation. Paper presented at: 2017 IEEE nuclear science symposium and medical imaging conference (NSS/MIC); October 21-28, 2017; Atlanta, GA.
17. Liu F, Jang H, Kijowski R, Zhao G, Bradshaw T, McMillan AB. A deep learning approach for 18F-FDG PET attenuation correction. *EJNMMI physics*. 2018;5(1):1-15.
18. Armanious K, Hepp T, Küstner T, et al. Independent attenuation correction of whole body [18F] FDG-PET using a deep learning approach with generative adversarial networks. *EJNMMI Res*. 2020;10(1):1-9.
19. Hashimoto F, Ito M, Ote K, Isobe T, Okada H, Ouchi Y. Deep learning-based attenuation correction for brain PET with various radiotracers. *Ann Nucl Med*. 2021;35:691-701.
20. Choi B-H, Hwang D, Kang S-K, et al. Accurate transmission-less attenuation correction method for amyloid-β brain PET using deep neural network. *Electronics*. 2021;10(15):1836.
21. Gandia-Ferrero MT, Torres-Espallardo I, Martínez-Sanchis B, et al. Objective image quality comparison between brain-dedicated PET and PET/CT scanners. *J Med Syst*. 2023;47(1):88.
22. Hwang D, Kim KY, Kang SK, et al. Improving the accuracy of simultaneously reconstructed activity and attenuation maps using deep learning. *J Nucl Med*. 2018;59(10):1624-1629.
23. Shiri I, Ghafarian P, Geramifar P, et al. Direct attenuation correction of brain PET images using only emission data via a deep convolutional encoder-decoder (Deep-DAC). *Eur Radiol*. 2019;29:6867-6879.
24. Dong X, Lei Y, Wang T, et al. Deep learning-based attenuation correction in the absence of structural information for whole-body positron emission tomography imaging. *Phys Med Biol*. 2020;65(5):055011.
25. Ouyang J, Chun SY, Petibon Y, Bonab AA, Alpert N, El Fakhri G. Bias atlases for segmentation-based PET attenuation correction using PET-CT and MR. *IEEE Trans Nucl Sci*. 2013;60(5):3373-3382.
26. Arabi H, Zaidi H. MRI-guided attenuation correction in torso PET/MRI: assessment of segmentation-, atlas-, and deep learning-based approaches in the presence of outliers. *Magn Reson Med*. 2022;87(2):686-701.
27. Arabi H, Bortolin K, Ginovart N, Garibotto V, Zaidi H. Deep learning-guided joint attenuation and scatter correction in multitracer neuroimaging studies. *Hum Brain Mapp*. 2020;41(13):3667-3679.
28. Zaidi H, Ojha N, Morich M, et al. Design and performance evaluation of a whole-body ingenuity TF PET–MRI system. *Phys Med Biol*. 2011;56(10):3091.
29. Bortolin K, Arabi H, Zaidi H, Deep learning-guided attenuation and scatter correction without using anatomical images in brain PET/MRI. Paper presented at: 2019 IEEE Nuclear Science Symposium and Medical Imaging Conference (NSS/MIC); October 26-November 2, 2019; Manchester, UK.
30. Burgos N, Thielemans K, Cardoso MJ, et al. Effect of scatter correction when comparing attenuation maps: application to brain PET/MR. Paper presented at: 2014 IEEE Nuclear Science Symposium and Medical Imaging Conference (NSS/MIC); November 8-15, 2014; Seattle, WA.
31. Watson CC. New, faster, image-based scatter correction for 3D PET. *IEEE Trans Nucl Sci*. 2000;47(4):1587-1594.
32. Jakoby B, Bercier Y, Conti M, Casey ME, Bendriem B, Townsend D. Physical and clinical performance of the mCT time-of-flight PET/CT scanner. *Phys Med Biol*. 2011;56(8):2375.
33. Gibson E, Li W, Sudre C, et al. NiftyNet: a deep-learning platform for medical imaging. *Comput Methods Programs Biomed*. 2018;158:113-122.
34. Li W, Wang G, Fidon L, Ourselin S, Cardoso MJ, Vercauteren T, On the compactness, efficiency, and representation of 3D convolutional networks: brain parcellation as a pretext task. Paper presented at: International conference on information processing in medical imaging 2017.
35. Tzourio-Mazoyer N, Landeau B, Papathanassiou D, et al. Automated anatomical labeling of activations in SPM using a

macroscopic anatomical parcellation of the MNI MRI single-subject brain. *Neuroimage*. 2002;15(1):273-289. Preprint posted online January 05, 2002.
36. Nioche C, Orlhac F, Boughdad S, et al. LIFEx: a freeware for radiomic feature calculation in multimodality imaging to accelerate advances in the characterization of tumor heterogeneity. *Cancer Res*. 2018;78(16):4786-4789. Preprint posted online July 01, 2018.
37. Ladefoged CN, Hansen AE, Henriksen OM, et al. AI-driven attenuation correction for brain PET/MRI: clinical evaluation of a dementia cohort and importance of the training group size. *Neuroimage*. 2020;222:117221.
38. Blanc-Durand P, Khalife M, Sgard B, et al. Attenuation correction using 3D deep convolutional neural network for brain 18F-FDG PET/MR: comparison with Atlas, ZTE and CT based attenuation correction. *PLoS One*. 2019;14(10):e0223141.
39. Ladefoged CN, Marner L, Hindsholm A, Law I, Højgaard L, Andersen FL. Deep learning based attenuation correction of PET/MRI in pediatric brain tumor patients: evaluation in a clinical setting. *Front Neurosci*. 2019;12:1005.
40. Arabi H, Zeng G, Zheng G, Zaidi H. Novel adversarial semantic structure deep learning for MRI-guided attenuation correction in brain PET/MRI. *Eur J Nucl Med Mol Imaging*. 2019;46(13):2746-2759.
41. Lei Y, Wang T, Dong X, et al. PET attenuation correction using non-AC PET-based synthetic CT. In: Guang-Hong Chen, Hilde Bosmans, eds. *Medical Imaging 2020: Physics of Medical Imaging 2020*. SPIE;2020.
42. Arabi H, Zaidi H. Truncation compensation and metallic dental implant artefact reduction in PET/MRI attenuation correction using deep learning-based object completion. *Phys Med Biol*. 2020;65(19):195002.
43. Yang J, Sohn JH, Behr SC, Gullberg GT, Seo Y. CT-less direct correction of attenuation and scatter in the image space using deep learning for whole-body FDG PET: potential benefits and pitfalls. *Radiol Artif Intell*. 2020;3(2):e200137.
44. Watson C. Extension of single scatter simulation to scatter correction of time-of-flight PET. *IEEE Trans Nucl Sci*. 2007;54(5):1679-1686.

SUPPORTING INFORMATION

Additional supporting information can be found online in the Supporting Information section at the end of this article.

How to cite this article: Jahangir R, Kamali-Asl A, Arabi H, Zaidi H. Strategies for deep learning-based attenuation and scatter correction of brain ^{18}F-FDG PET images in the image domain. *Med Phys*. 2024;51:870–880. https://doi.org/10.1002/mp.16914